Tectonic Aneurysm and Mountain Building

Peter O Koons[1], Peter Zeitler[2], Bernard Hallet[3]
[1]University of Maine, [2]Lehigh University, [3]University of Washington

Abstract

Some of the most spectacular topography on the planet arises from the product of localized interactions between climate, erosion and tectonics. A notable example emerges when climate and tectonic systems mutually influence their thermal structures. In the atmosphere this influence can lead to orographic effects that focus precipitation, which is funneled by rivers and glaciers into spatially restricted zones with a high potential for erosion. Focusing of this erosional power onto the solid Earth at deforming convergent margins then perturbs stress fields and the material properties of the lithosphere, diverting the three-dimensional tectonic velocity field. The resulting rapid ascent of crustal material produces a hot and correspondingly weak domain in the upper crust. This weak domain further concentrates strain, generating the zone of stable, rapid uplift and exhumation that we refer to as a tectonic aneurysm. The tectonic aneurysm is characterized by extreme relief where rapid exhumation has been sustained (for 3 Myr or more) and very young metamorphic assemblages are exposed adjacent to exceptionally powerful fluvial (~200 kW/m or more) or glacial (~40 kW/m) erosional agents. This characteristic ensemble of metamorphic, surface, and tectonic features, that together constitutes the tectonic aneurysm, are present to varying degrees in the three examples that we review: Nanga Parbat, northwest Pakistan; Namche Barwa, southeast Tibet; and St Elias, southeast Alaska. Petrologic, geomorphic, and geodynamic investigations of these three extreme regions, summarized here, illuminate the non-linear interaction and cooperative behavior of tectonics and surface processes, which are likely universal, but are most clearly manifested in these regions where the high process rates produce a high signal to noise ratio.

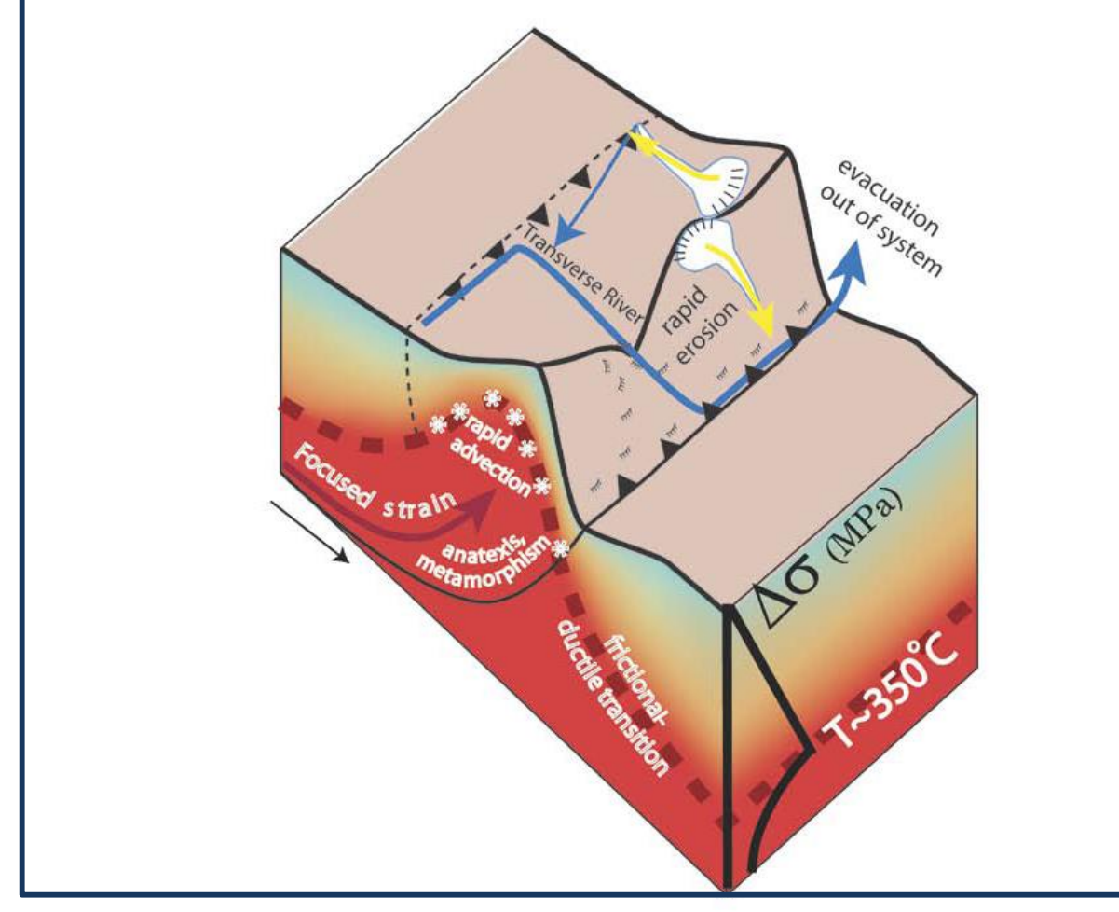

Figure 1.
Schematic representation of the fully evolved tectonic aneurysm, (modified from Zeitler et al., 2001a). Rapid advection along particle trajectories indicated by arrows leads to both topographic, thermal, and rheological anomalies. The rheology of the pressure-dependent upper crust resting on a thermally activated lower crust is represented by Δσ the transition at ~ 400°C (Brace and Kohlstedt, 1980).

Figure 2.
Three tectonic aneuryms:
a) North face of Nanga Parbat massif as seen from the Indus valley (view is from north). The Indus River in the middle distance (~1100 m above sea level (masl) and the summit (8126 masl) define 7 km of relief over < 25 km horizontally.
b) West face of Namche Barwa rising from the Tsangpo in the left at <3000 masl to the summit (7782 masl) in a horizontal distance of < 12 km. **c)** St Elias (5429 masl) ~ 20 km from the Gulf of Alaska with the terminus of the piedmont glacier, Malaspina in the foreground (photo: S. Campbell).

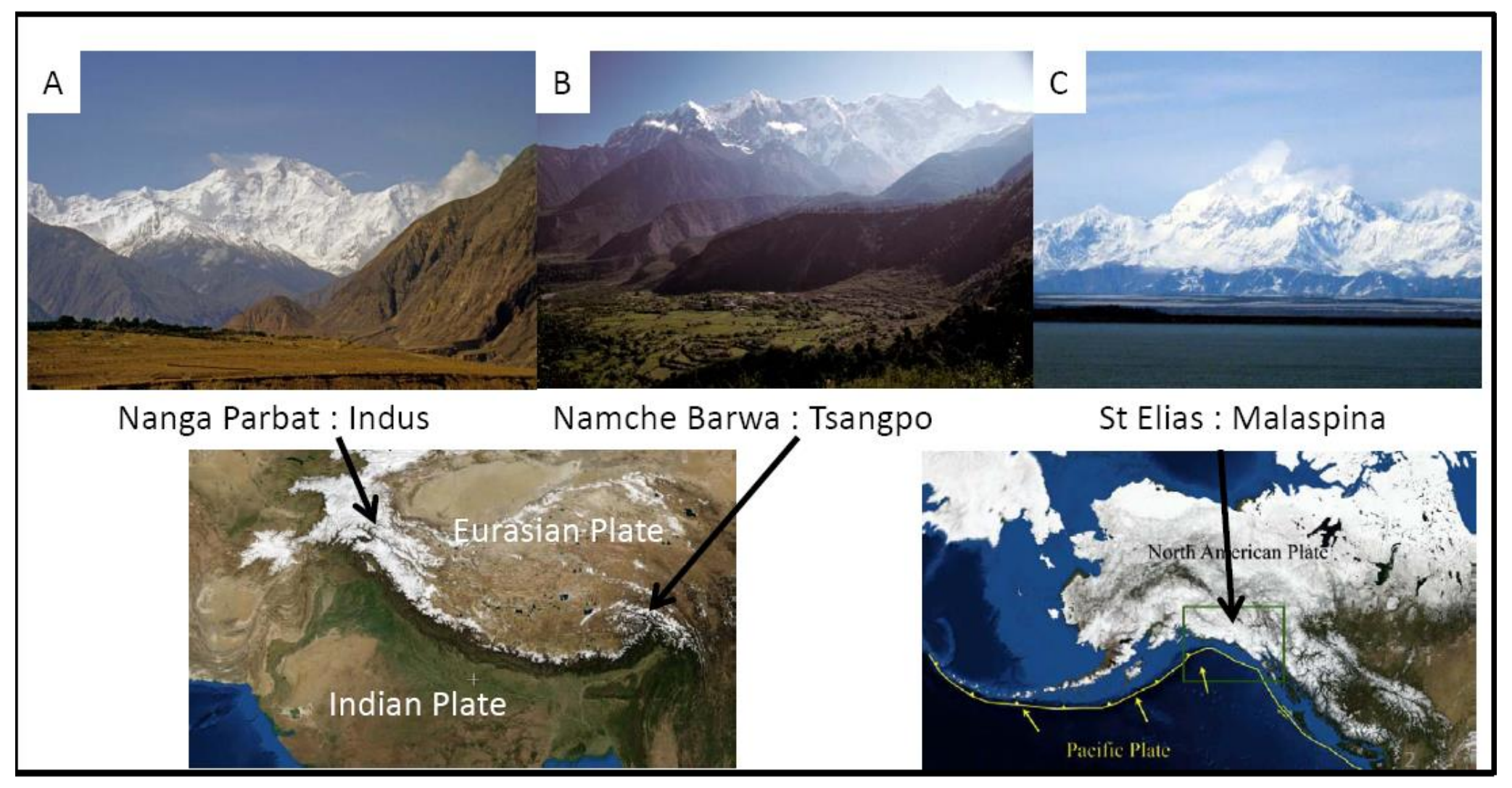

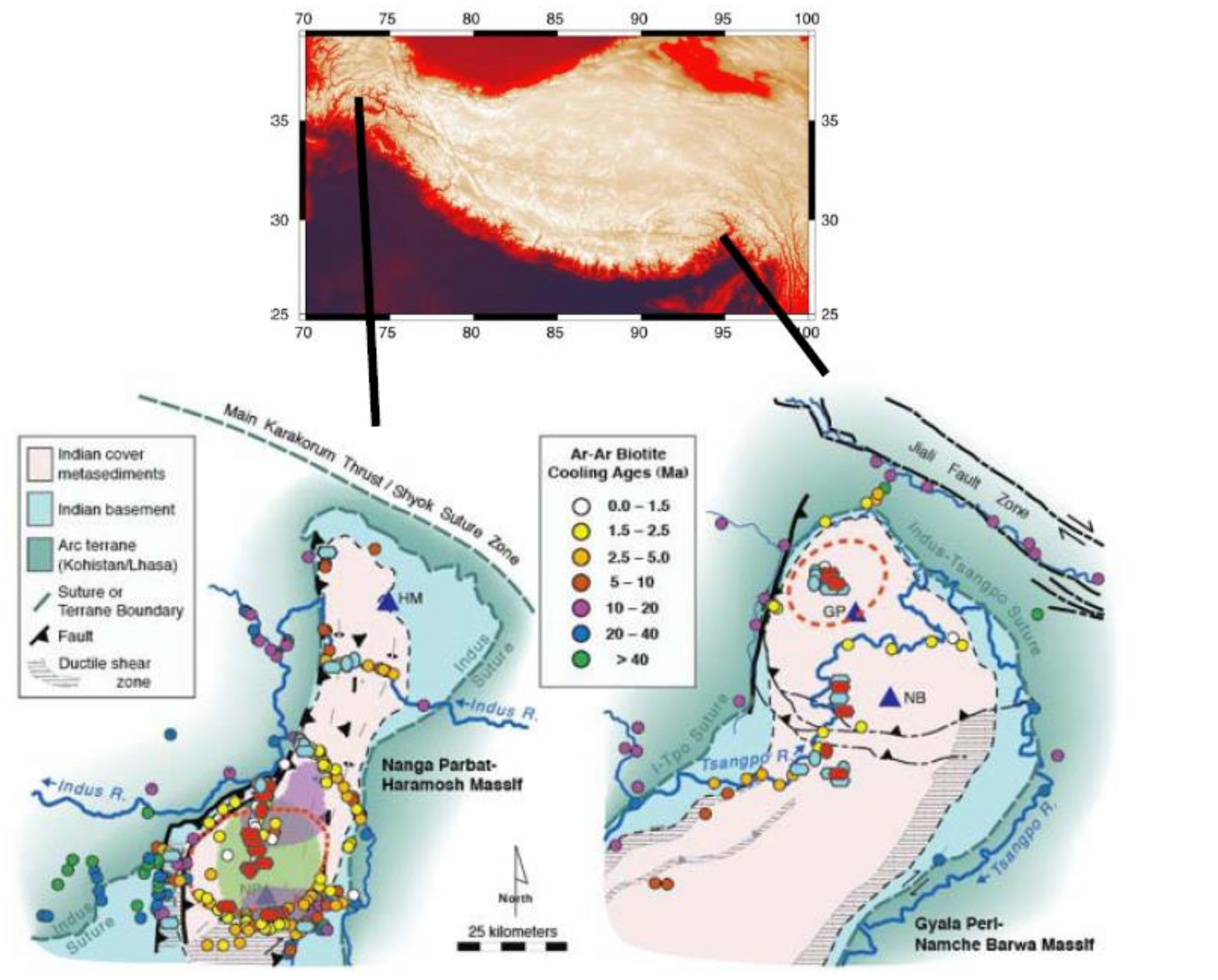

Figure 3.
Comparison of geological observations of the Nanga Parbat and Namche Barwa aneurysms, drawn to the same scale. The dashed red line encloses exposures of low-pressure granulites. At Nanga Parbat, the purple regions show the surface projection of anomalously low S-wave velocities at depth; the green region shows the location of a similar anomaly observed for P-waves. Note that the regions of very young cooling ages and inferred rapid exhumation have nearly the same area for each locality. Not also the coincidence between young cooling ages, young U-Pb ages, low-P granulite metamorphism, the active bounding thrusts, and the geophysical anomalies. Geological observations are
from Schneider *et al.* (1999), Zeitler *et al.* (2001b), and Booth *et al.* (2009). The geophysical data are from Meltzer *et al.* (2001). For Nanga Parbat, cooling-age data are from compilations by Schneider *et al.* (2001), Treloar *et al.* (2000), and George *et al.* (1995), and U-Pb data are those compiled in Zeitler *et al.* (2001b). For Namche Barwa, cooling ages are those reported in Stewart *et al.* (2008) and the U-Pb data from Booth *et al.* (2004; 2009) and Burg *et al.* (1998).

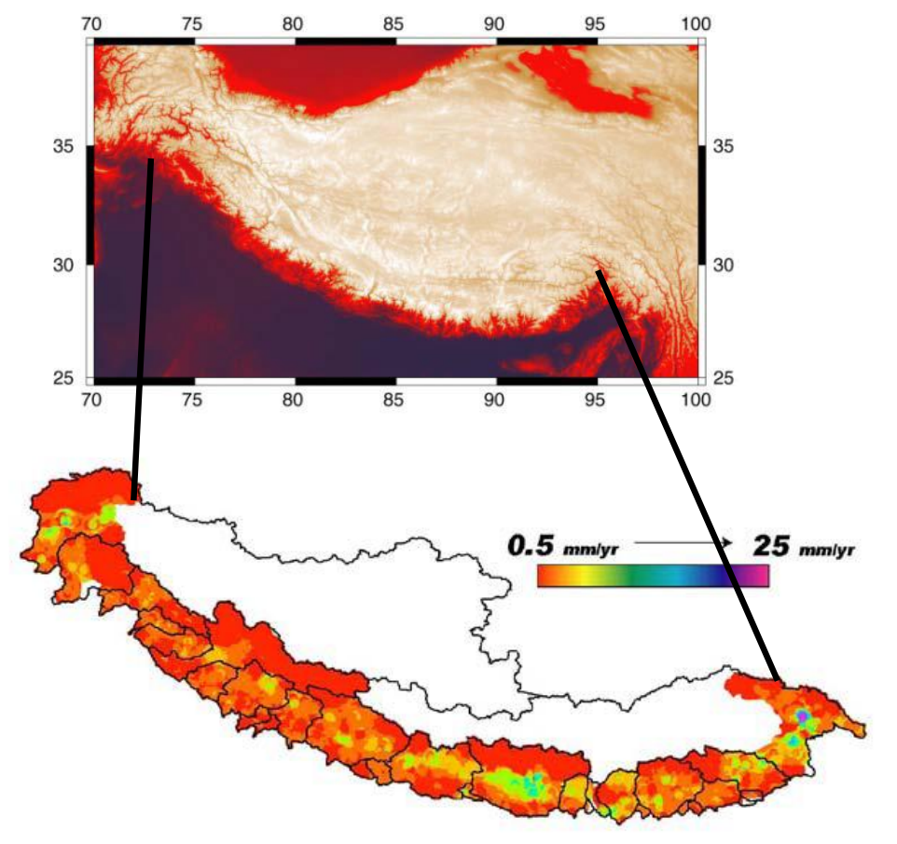

Figure 4.
Index of fluvial erosion rates illustrating schematically the spatial variation in potential erosion rates throughout the Himalaya. The index is the river power, the product of river discharge and slope; it has been expressed very roughly in terms of erosion rates using a Himalaya-wide comparison of river power and diverse erosion and exhumation data, assuming a highly idealized range where all other parameters controlling river incision show insignificant spatial variation on the scale of the range. See Figure 14 for more precise maps of river power. The river discharge was estimated here from generalized maps of precipitation (Finlayson *et al.*, 2002) and a coarse digital elevation model (GTOPO-30). Courtesy of D. Finlayson.

Figure 8.
Modern effective erosion rates derived from sediment yields from glaciated basins in coastal Alaska (red symbols) versus unglaciated fluvial basins worldwide (other colors from global compilation of Milliman and Syvistky, 1992); data were first presented by Hallet *et al.* (1996). The red symbols represent estimates of erosion rates over periods longer (large circles) and shorter (small circles) than a decade. For Alaskan tide-water glaciers, these estimates are conservative because measured contemporary sediment yields were divided by a factor of five to account liberally for systematic bias associated with current glacial retreat throughout the region (e.g. Koppes and Montgomery, 2009; Koppes *et al.*, 2009). Large glacial basins generally produce more sediment than other major basins including those identified as having the highest sediment yields by Milliman and Syvitski (1992), and basins in British Columbia (Slaymaker, 1987) and Himalaya (Delcaillau, 1992).

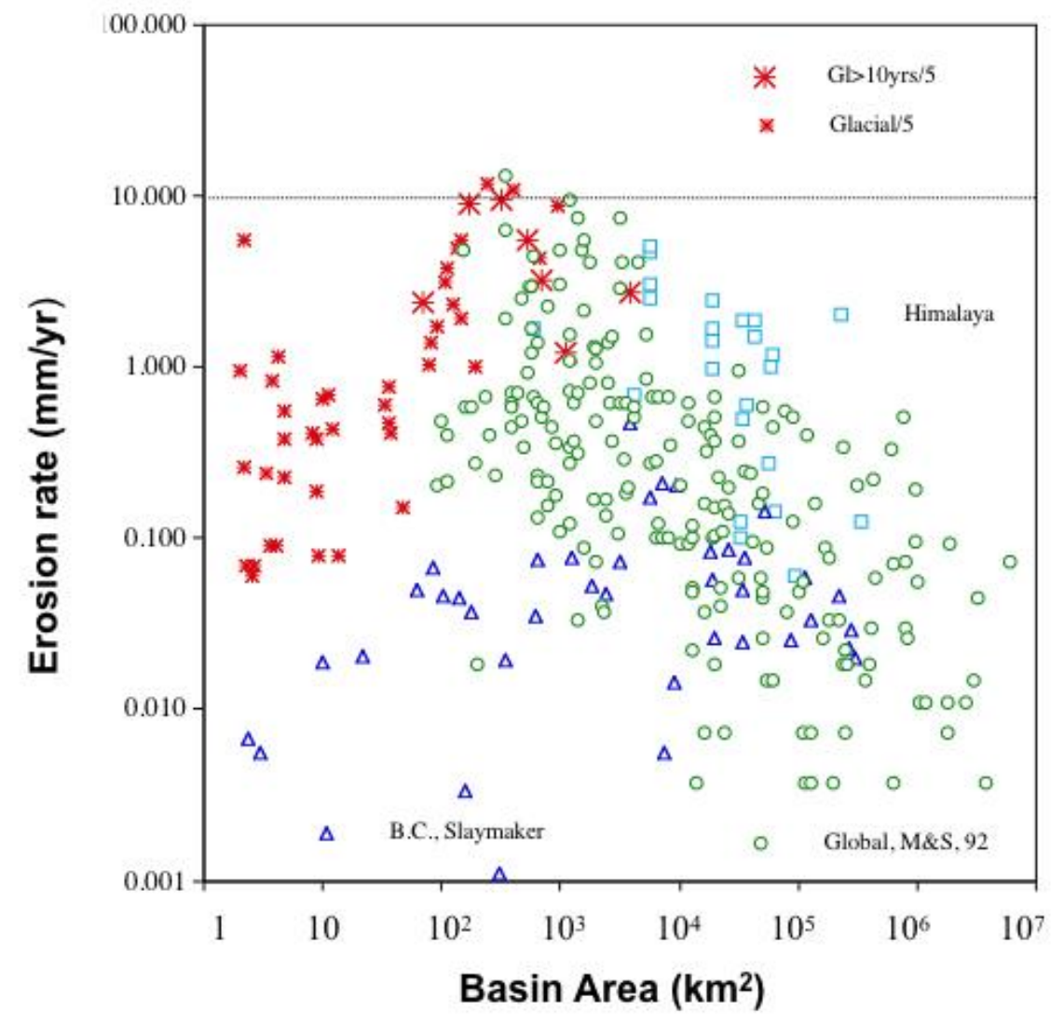

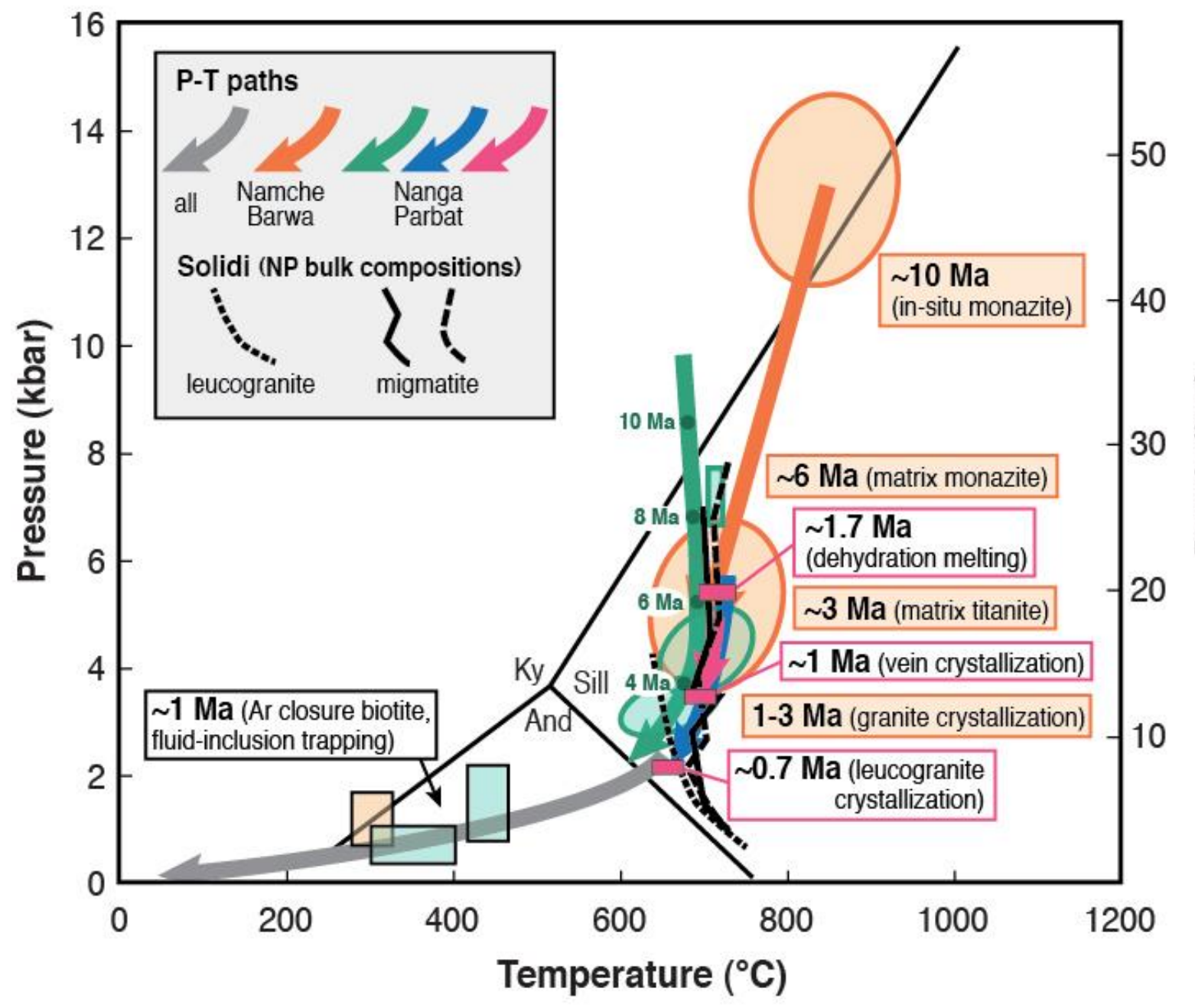

Figure 9.
Summary in *PTt* space of petrological observations at Namche Barwa and Nanga Parbat. Rocks from both massifs show strong decompression paths that pass through the low-pressure granulite field, consistent with model predictions for exhumation rates of several mm/yr or higher. Nanga Parbat petrological data are from Whittington *et al.* (1999a,b; *PT* observations and model *PT* path, in green) and from Crowley *et al.* (2009) (U-Pb dates, *PT* data and inferred *PT* path from two migmatite samples, magenta and blue). Namche Barwa petrological and U-Pb data are from Booth *et al.* (2009; orange). The filled boxes at low temperatures and pressures are fluid-inclusion observations from Craw *et al.* (2005; Namche Barwa, orange) and Winslow *et al.* (1994; Nanga Parbat, green). Solidi were calculated by Crowley *et al.* (2009) for bulk compositions of a Nanga Parbat leucogranite and two different migmatite samples.

Figure 10.
Tectonic sketch map of SE Alaska, summarizing results from fission-track dating of detrital zircons. Significant populations of young zircons are present only in sand samples from the margins of the Malaspina Glacier, suggesting a very localized source area. Warping of structural trends shows location of the region above the indentor corner developed due to the collision of southern Alaska with the Yakutat terrane. After Enkelmann *et al.* (2009).

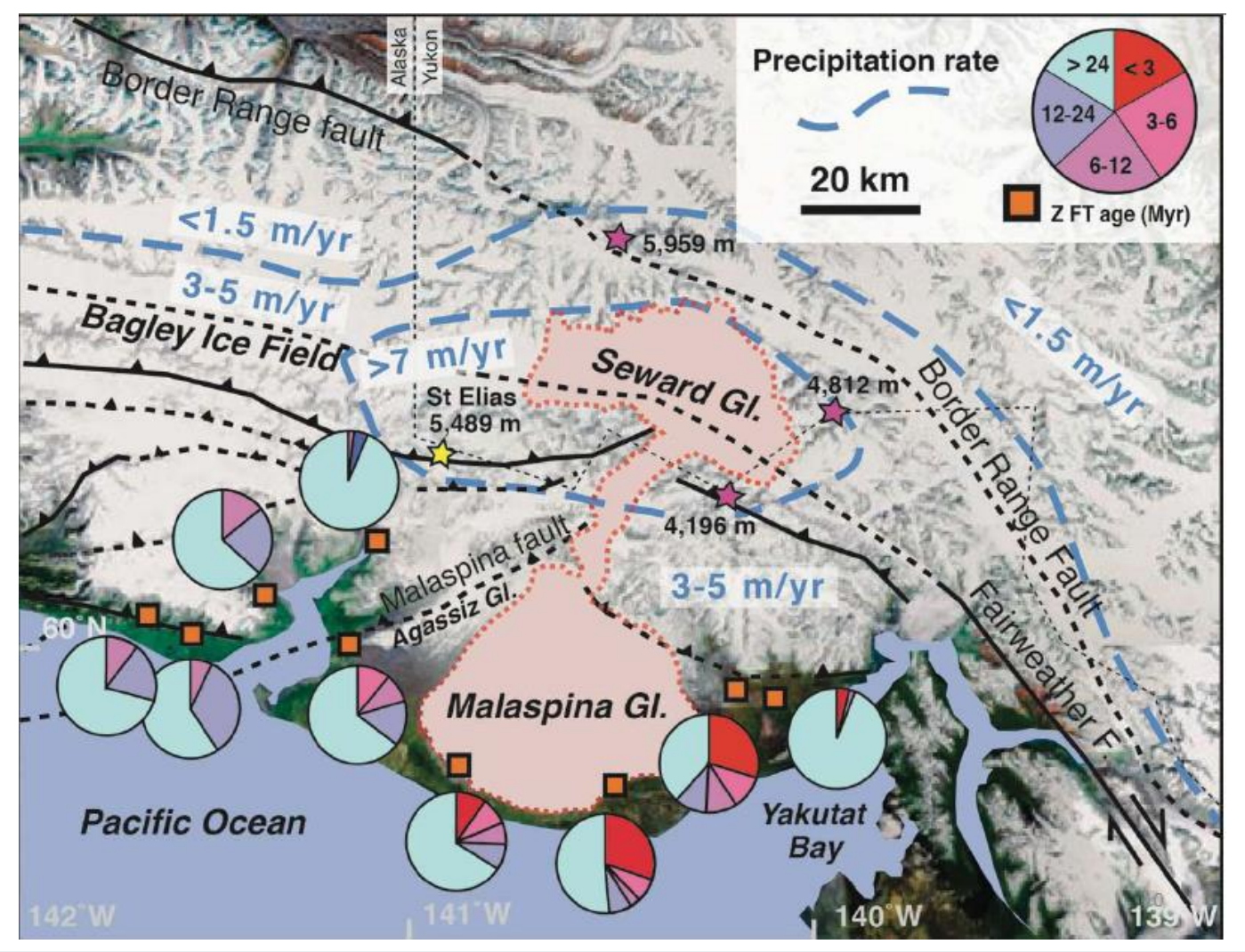

Figure 12.
Geologic manifestation of a fully developed tectonic aneurysm, based on observations at Nanga Parbat and Namche Barwa. In the presence of regional compressive strain (1), older, previously metamorphosed basement rocks enter the local system and encounter high strain associated with deformation within the aneurysm (2), possibly leading to additional devolatilization. As these rocks are rapidly uplifted along steep reverse-fault systems they experience rapid decompression and undergo dehydration melting (3) and low-pressure metamorphism (4), leading to formation of migmatites and granite dikes and bodies. Rapid advection of rock significantly uplifts isotherms and the brittle-ductile transition (5), steepening the geotherm and locally weakening the crust. In conjunction with rapid erosion, this results in the development of high mountains atop weak crust (6); this high topography and large relief in turn supports rapid erosion (7) by glacial carving and mass wasting. Eroded material is carried out of the system by large orogen-crossing rivers. The steep geothermal and large topographic head driveextensive meteoric-water circulation systems (8) above the brittle-ductile transition; a small fraction of this water may be kneaded to greater depths along shear zones (9) and could contribute to melting and vein development.

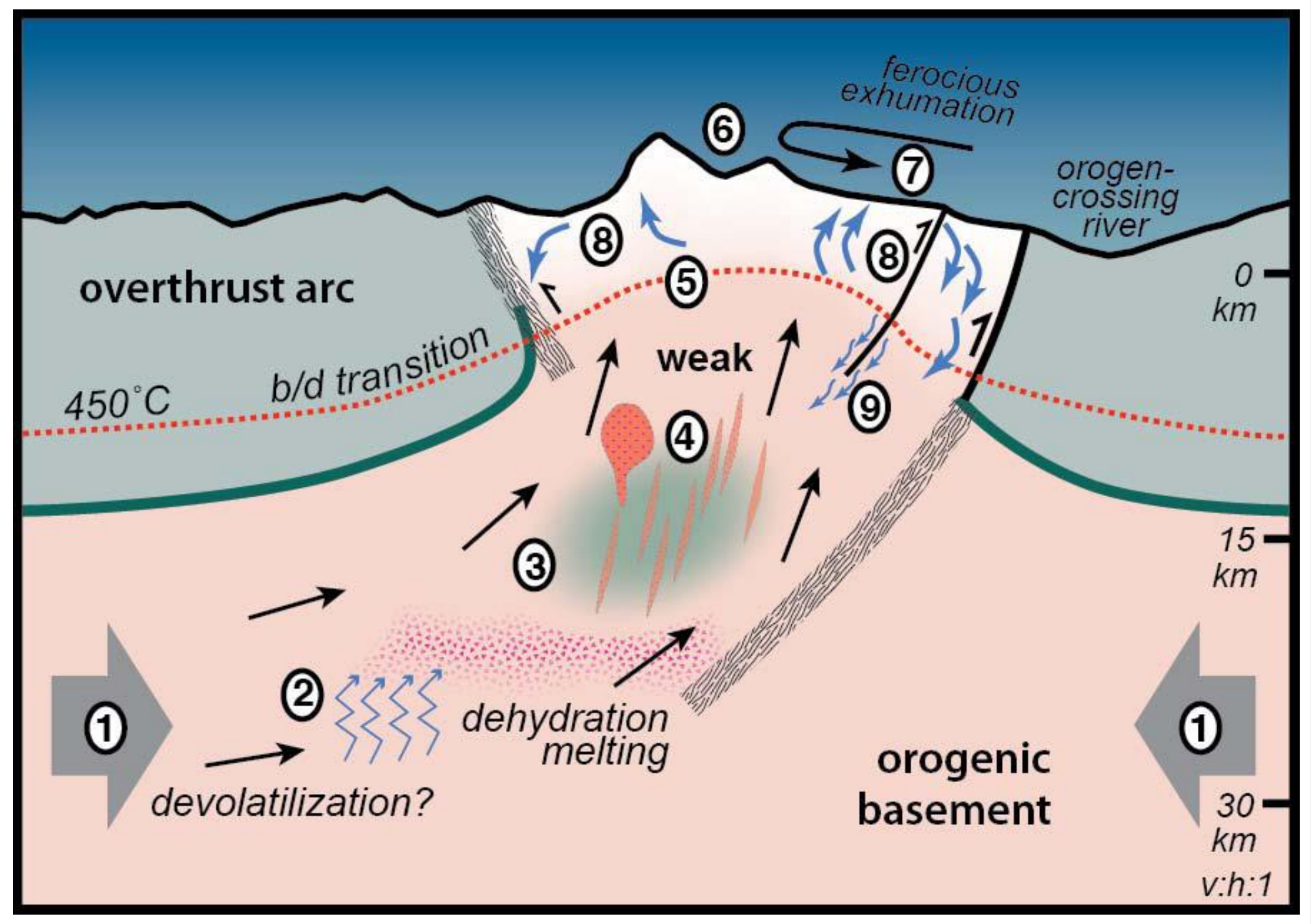

Figure 14. River power per unit river distance (in kW/m) along principal rivers in the Himalaya.
a) Orange and red colors signal location and extent of the eastern Himalayan tectonic aneurysm, a highly localized domain (roughly 0.5% of ~106 km2 region) centered on Namche Barwa that coincides with known area of rapid exhumation.

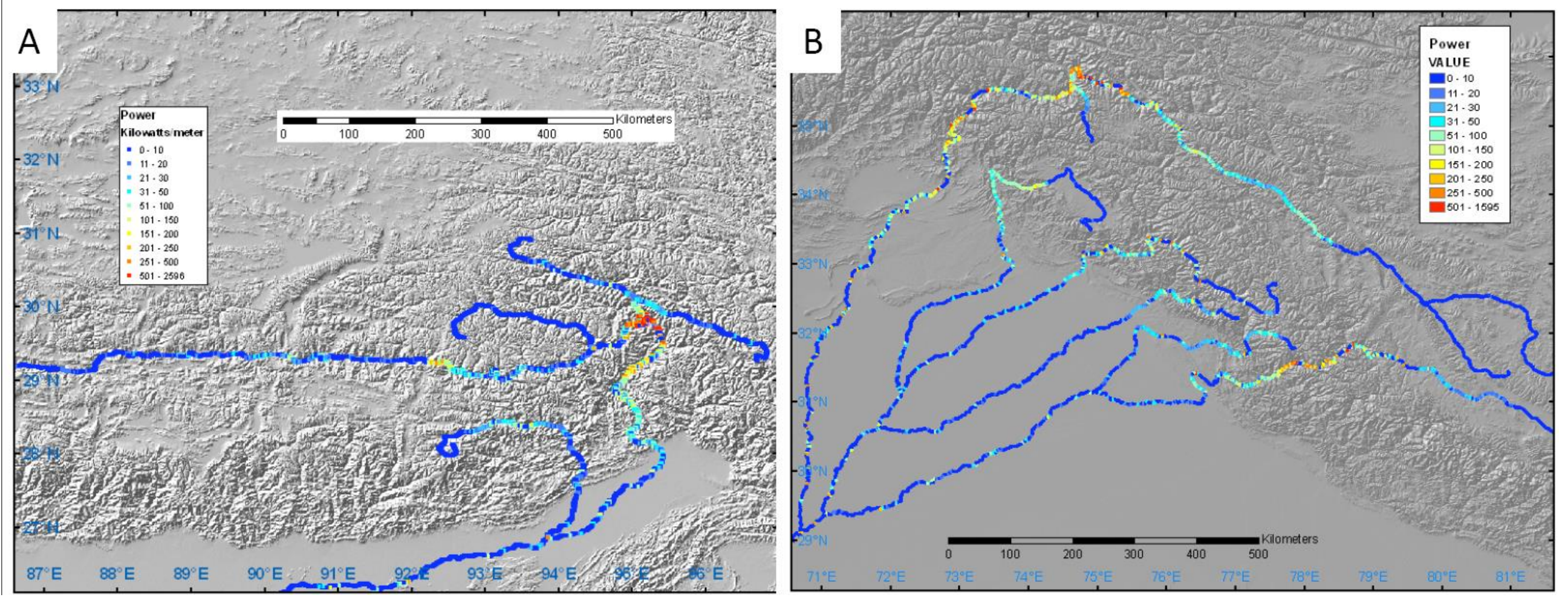

b) River power is also exceptionally high along main Indus (northern most river) where it slices through the western tectonic aneurysm, which includes Nanga Parbat. Energetic river reaches also occur along the southern-most tributary, which is the Sutlej. Interestingly, these reaches extend from about 77 to 79ºE, which coincides with a region of rapid exhumation defined by apatite fission-track ages of less than 2 Ma (Figure 1 in Thiede *et al.* 2005). River power computed from annual discharge estimated from 8 years of TRMM precipitation data, and 4-km averaged river slopes from ASTER DEMs. Courtesy of H. Greenberg.

Figure 15
a) Surface ice velocities for Seward-Malaspina glacier system; inset shows location in Alaska. Massive amounts of ice from the Seward icefield funnel south through the Seward Throat, a narrow gap in the range that culminates in Mt. St. Elias, and then spreads out into the large piedmont lobe defining Malaspina glacier. The velocities, derived from satellite data by E. Rignot, approach 2 km/yr in the Seward Throat. The flowband used in a glacier dynamic analysis by R. Headley is highlighted, and the pink star marks the one site of known ice thickness. Major faults labeled in italics (CSEF: Chugach St. Elias thrust fault), and glaciers are in bold. Courtesy of R. Headley.

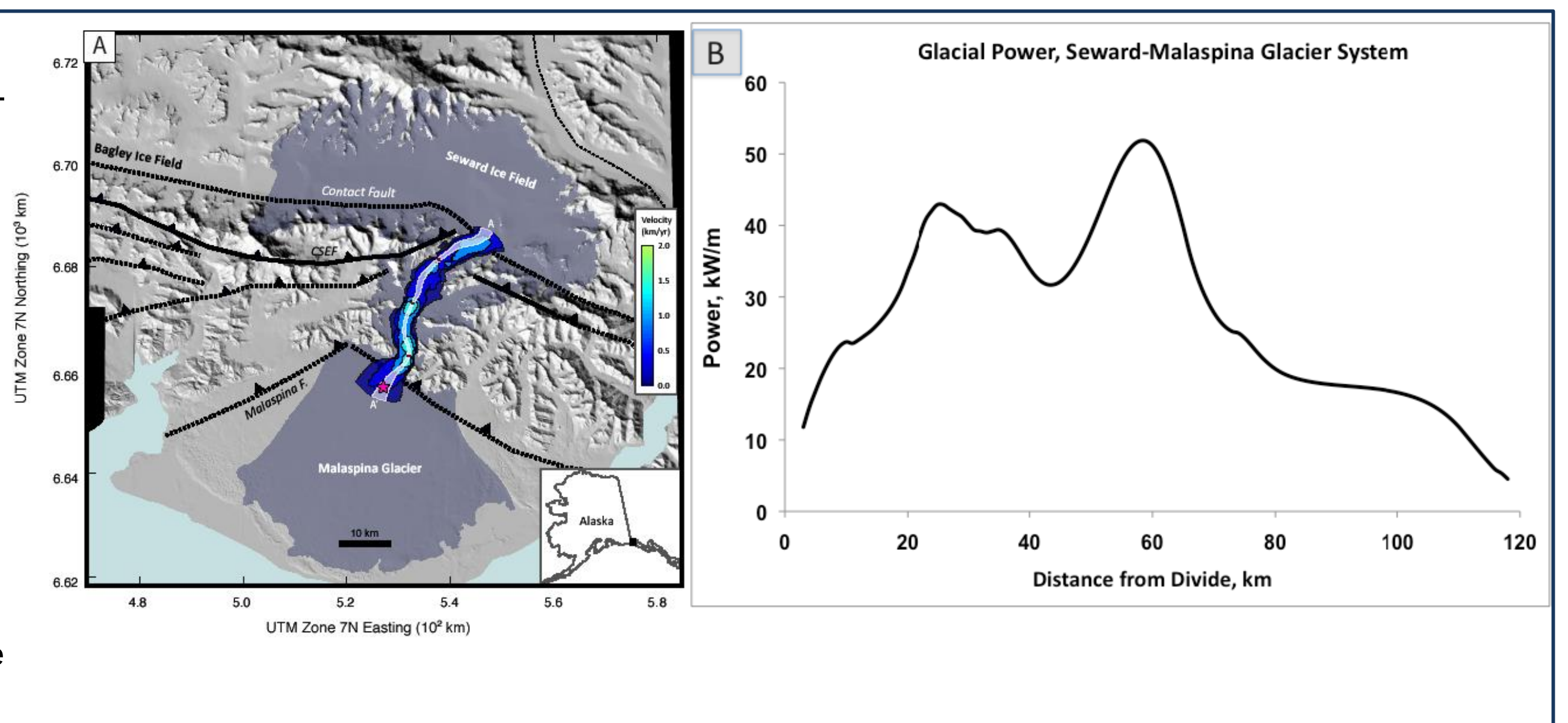

b) Generalized glacier power per unit distance down-glacier, guided by glacier dynamic analysis, shows strong peak in the Seward Throat area where rapid ice flow and high shear stresses, between 25 and 70 km, combine to produce exceptionally high basal power. Correspondingly, rapid erosion is expected in this energetic region, and fast local uplift must offset the rapid erosion for this system to be sustained.

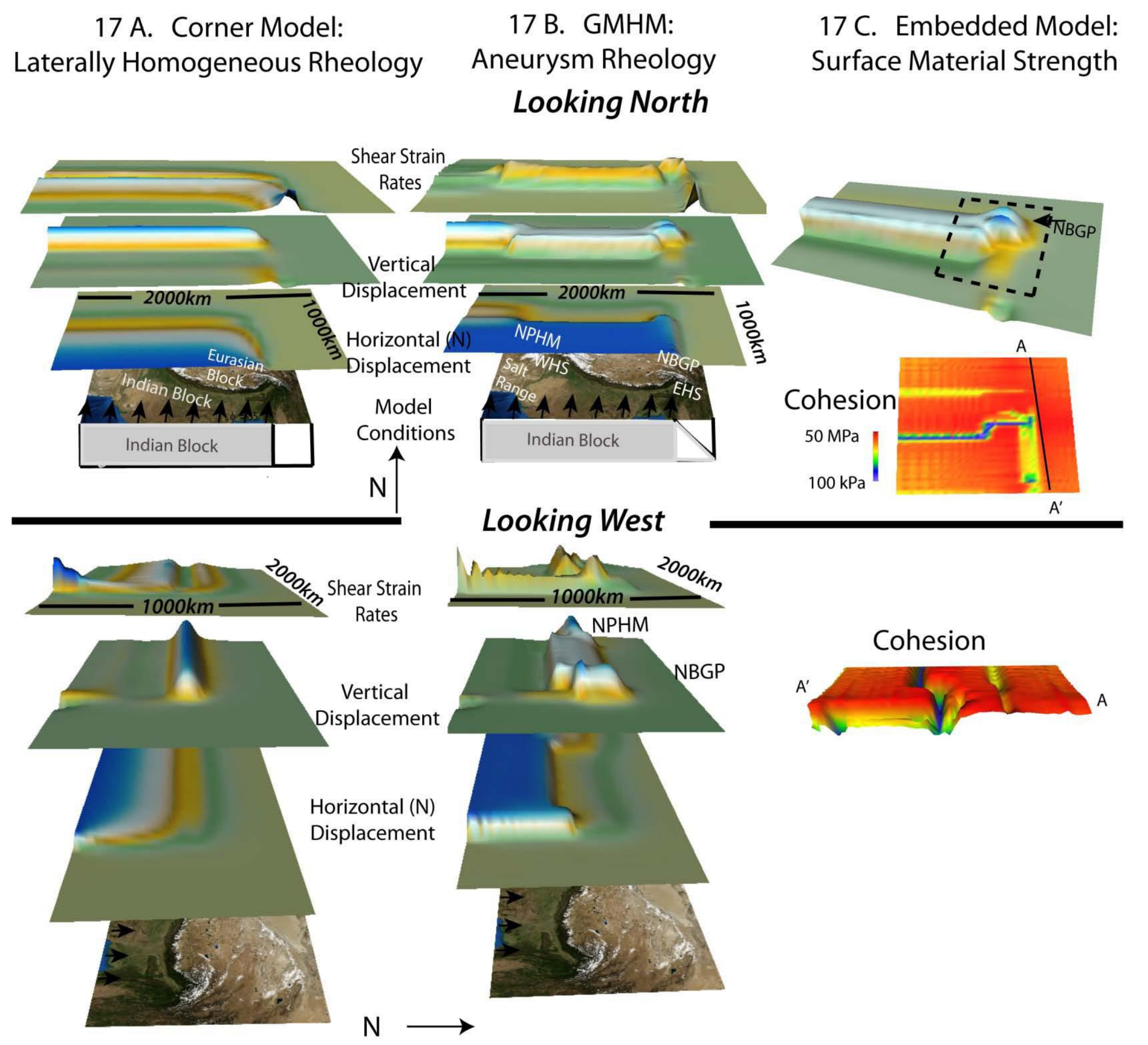

Figure 17.
North and West looking views of 3D mechanical investigation of the influence of erosion-induced rheological perturbations characteristic of tectonic aneurysm behavior on the kinematics and topography of the Himalayan orogen.
a) Corner Model: convergence of India lithosphere into Eurasia with laterally homogeneous rheology. Surfaces depict x-displacement, z-displacement and shear strain rates at the model surface as labeled. In these and following figures, maximum values are in blue, and stand out in relief. See text for discussion.
b) GMHM Model of same geometry and influx velocities as in a) *Corner Model*, but with rheological modifications associated with the non-linear coupling described in section 2. Note the northward re-entrant at both syntaxes. Surfaces depict x-displacement, z-displacement and shear strain rates at the model surface as labeled.
c) Embedded Model of Eastern Syntaxis with strain softening upper crustal rheology. Strain concentration leads to surface strength reduction pattern represented by the model cohesion field at the orogen surface that exhibits the distinctive northward step observed in the EHS. (Details in Koons *et al.*, 2011).

Figure 18.
Three-dimensional summary models of the geodynamics of the St Elias region in southern Alaska.
a) Macroscale Model (Details in Koons *et al.*, 2010). Geometry of the plate boundary derived from Pavlis *et al.*, 2004; Hooks, 2009, Koons *et al.*, 2010) Convergence of the Yakutat plate at Pacific plate far field velocities (Elliott *et al.*, 2010). Vertical velocity pattern defined by maxima at inflow and outflow boundaries with concentration along the trasition between inflow and lateral boundaries of model *St Elias* where the strain trinity accommodates the complex deformation.
b) Embedded Model (Details in Hooks, 2009; Hooks *et al.*, 2011) Model vertical velocities (red; mm/yr) are superimposed on the thermochronological observations presented in Figure 10. Highest model velocities coincide with the Seward Glacier.